Soils and Foundations 2012;52(4):658–667

The Japanese Geotechnical Society

Soils and Foundations

www.sciencedirect.com
journal homepage: www.elsevier.com/locate/sandf

Determination of mobilized strength properties of degrading sandstone

Mahshid Jafarpour[a,*], Hossein Rahmati[a], Saman Azadbakht[a], Alireza Nouri[a], Dave Chan[a], Hans Vaziri[b]

[a]*Department of Civil and Environmental Engineering, University of Alberta, Edmonton, Alberta, Canada*
[b]*BP America Inc., Houston, TX, United States*

Received 22 June 2011; received in revised form 9 May 2012; accepted 25 May 2012
Available online 9 August 2012

Abstract

This paper describes a method for calibrating elasto-plastic models based on the results of triaxial tests on two types of sandstones. Emphasis is given to the simulation of the softening regime of the stress–strain response of the material with special attention to minimizing mesh-dependency. A pragmatic and easy-to-implement procedure is developed for the calibration under the framework of friction hardening/cohesion softening. Fracture energy regularization is applied in the back-analysis of the triaxial tests to remove mesh dependency. The impact of different mesh designs is investigated. Oriented mesh with the same inclination as the shear band provides the most realistic outcome and is able of capturing real shear band thickness.
© 2012 The Japanese Geotechnical Society. Production and hosting by Elsevier B.V. All rights reserved.

Keywords: Calibration; Fracture energy regularization; Localization; Sandstone; Shear band; Softening

1. Introduction

Sandstone is a granular material with cementation that shows frictional and dilatancy behavior. Modeling engineering structures requires the ability to capture full development of damages in the sandstone. In these analyses, it is essential to accurately describe the hardening/softening behavior normally observed in sandstone. Sulem et al. (1999) showed that sand behavior can be modeled using the friction hardening and cohesion softening concept using the Mohr–Coulomb model. Later, Nouri et al. (2009) adopted the same approach for calibration, but used a bilinear Mohr–Coulomb yield surface instead of a linear one. Sulem's work assumes uniform deformation in triaxial tests and produces questionable results by neglecting localization of deformation.

Simulation of the post-peak response of geomaterials using continuum-based models has been observed to produce results that are spuriously dependent on the numerical mesh design. The continuum model must be modified by a regularization method to reduce or eliminate mesh dependency (Crook et al., 2003). Regularization can be carried out by incorporating a characteristic length scale into the formulation. The characteristic length depends on the material, and it is usually related to the grain sizes of the granular material. Methods such as Cosserat continuum, gradient plasticity and non-local models have been used to address the

*Corresponding author.
E-mail address: mashid@ualberta.ca (M. Jafarpour).
Peer review under responsibility of The Japanese Geotechnical Society.

Production and hosting by Elsevier

0038-0806 © 2012 The Japanese Geotechnical Society. Production and hosting by Elsevier B.V. All rights reserved.
http://dx.doi.org/10.1016/j.sandf.2012.07.007

Nomenclature

ECS	effective confining stress
HECS	high effective confining stress
LECS	effective confining stress
C	cohesion
c^P	peak cohesion
c^*	mobilized cohesion in the softening
d_{50}	average grain size
E	Young modulus
e_r	radial strain
e_z	axial strain
$\dot{e}_1^p$	plastic axial strain rate
$\dot{e}_v^p$	plastic volumetric strain rate
F	yield function
h_p	hardening parameter
$\dot{h}_p$	hardening parameter rate
hp^p	peak hardening parameter
J_2	the second invariant of the deviatoric stress
P	mean stress
q	tension cut-off
q_i	initial yield tension cut-off
q_P	peak tension cut-off
q_r	residual tension cut-off
q^H	tension cut-off at HECS
q^L	tension cut-off at LECS
S_{ij}	deviatoric stress
T	$\sqrt{J_2}$
t_s	shear band thickness
μ	friction coefficient
μ^H	friction coefficient at HECS
μ^L	friction coefficient at LECS
υ	Poisson's ratio
σ'_r	effective radial stress
σ'_z	effective axial stress
φ	friction angle
φ_{cv}	constant volume friction angle
ψ	dilation angle

mesh-dependency problem. However, the Cosserat method is effective as a regularization method when frictional slip is prevailing (Sluys, 1992). Gradient plasticity regularization is applicable as long as the shear band is thicker than the element size thus requiring a very fine mesh in many cases. Non-local models are computationally intensive when modeling field-scale applications. Fracture energy regularization developed by Pietruszcak and Mroz (1981) and Bazant and Oh (1983) among others is applied here. This method also has its limitation: the characteristic length of the element must be larger than the material characteristic length. However, this is of little consequence for field applications (Crook et al., 2003).

In this paper, a few modifications and simplifications have been incorporated into Sulem's work to ensure the calibration procedure is easy to implement, objective and efficient in capturing rock behavior.

Bilinear Mohr–Coulomb yield surface is used, which was also adopted by Nouri et al. (2009). Emphasis is given here to simulating the softening behavior of the material. Sulem's work is based on the uniform deformation in a triaxial test, an assumption which is highly violated in the softening regime where localization occurs. Hence, the approach proposed by Vermeer, De Borst (1984) was adopted for modeling the softening regime. They calibrated the softening regime using an exponential function with a tuning parameter to match the experimental data. Fracture energy regularization is also employed to enhance the Mohr–Coulomb model. In addition, oriented mesh with an inclination equal to the expected rock failure angle is used. This special mesh design limits the localized deformation to only one element size so that the shear band thickness is produced numerically. The model calibration is applied to two different sandstones (Castlegate and TB sandstones). Back-analysis of the results is then conducted to ensure the calibrated formulations can predict the experimental results. The effect of mesh design is discussed, and the results are compared with the results of the regular mesh design.

2. Experimental data

The results of 16 triaxial tests on sandstone core samples taken from a petroleum reservoir, referred to as TB in this paper, are utilized. The samples were taken from different depths and at different temperatures and orientations with respect to the bedding plane. Four out of the 16 tests are selected for this calibration task. All samples for these four tests were taken from the same depth, and the tests were carried out at a temperature of 21.11 °C (70 °F). The core plugs were taken with the plug axis perpendicular to the bedding plane. Six triaxial tests were conducted on Castlegate sandstone. In these tests, the sample was first loaded isotropically to the confining stress level, after which only axial loading was applied with constant radial stress.

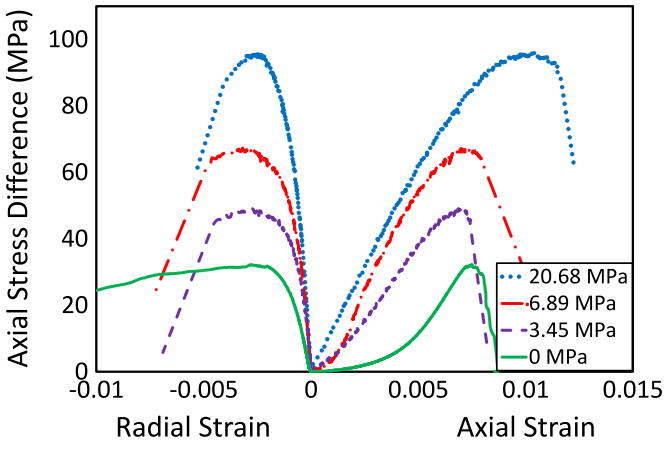

Fig. 1. Experimental triaxial data on TB at different effective confining stresses (ECS).

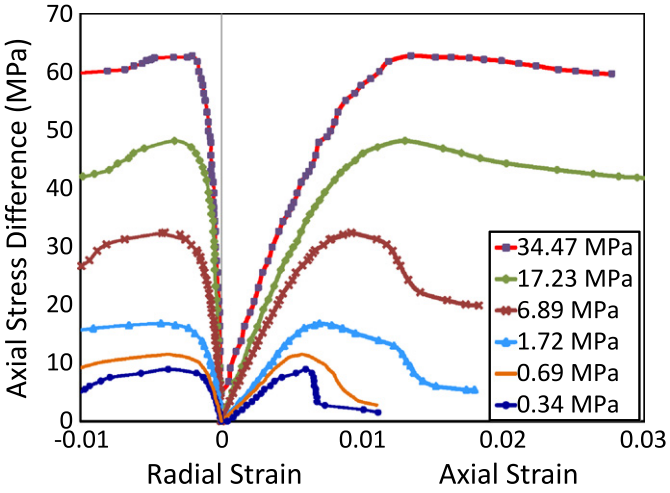

Fig. 2. Experimental triaxial data on Castlegate at different ECS.

The stress–strain responses are shown in Figs. 1 and 2. Each curve shows the response at a different confining stress.

Figs. 1 and 2 show the average radial strains measured at two points 90° apart on the outer surface and in the mid-height of the samples. Both TB and Castlegate sandstones are used in the calibration which will be disussed later.

3. Theory and formulation

3.1. Elastic properties

Stress-dependent elasticity is commonly observed in sandstone and more generally in granular materials. For simplicity and due to a lack of unloading data, however, elastic parameters are assumed to depend on the confining stresses, but not on the plastic strain. Due to a lack of unloading data, the error in the selection of the initial yield point is inevitable. Elastic properties are determined at 50% of the peak stress (see Fig. 3) as recommended by Schanz et al. (1999). Poisson's ratio can be calculated using the definition of: $\upsilon = -e_r/e_z$, and the Young modulus is calculated by

$$E = \frac{q}{e_z} \tag{1}$$

Sulem et al. (1999) emphasized the significance of calibration of the elastic moduli since they not only affect the elastic calculations, but they also influence the calculation of the plastic strains considerably.

3.2. Yield surface

The yield function implemented is a bilinear Mohr–Coulomb model which was also used by Nouri et al. (2009). Fig. 4 shows the yield surface in a T–P plot where T is the square root of the second invariant of the deviatoric stress tensor, and P is the mean effective stress. For a triaxial test

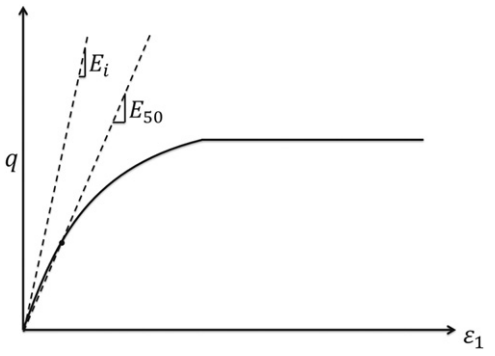

Fig. 3. Secant stiffness modulus at 50% of the peak loading, E50 (Schanz et al., 1999).

condition, they are simplified as

$$P = \frac{\sigma'_{ii}}{3} = \frac{\sigma'_z + 2\sigma'_r}{3} \tag{2}$$

$$T = \sqrt{J_2} = \sqrt{\frac{1}{2} S_{ij} S_{ji}} = \frac{|\sigma_z - \sigma_r|}{\sqrt{3}} \tag{3}$$

The yield surface equation is bilinear with each line described by

$$F = T - \mu(q + P) = 0 \tag{4}$$

where μ is the friction coefficient and has the following relationship with the mobilized friction angle for the axisymmetric state of stress:

$$\mu = \frac{2\sqrt{3}\sin\phi}{3 - \sin\phi} \tag{5}$$

and q is the tension cut-off which can be related to the mobilized cohesion, C, by the following relationship:

$$q = \frac{C}{\tan\phi} \tag{6}$$

The behavior of sandstone is schematically demonstrated in Fig. 4. The hardening behavior is shown in Fig. 4a where line (0) shows the initial yield surface. Once a stress state reaches line (0), plastic deformation begins. Further loading increases the friction coefficient or the slope of the line up to the peak yield surface (line (1)). This is shown by the upward arrows from line (0) to line (1). Up to this point, the tension cut-off is approximately constant both for the low and high effective confining stresses ($q_i^L \approx q_P^L$ and $q_i^H \approx q_P^H$). Additional deformation after the peak results in the softening of the material and shrinkage of the yield surface. This is demonstrated in Fig. 4b by the downward arrows from line (1) to line (2). During softening, tension cut-off shrinks to the residual value (q_r), and it is equal to zero for fully degraded sandstone, as depicted in Fig. 4b. However, the friction coefficient remains constant. That is, the line is lowered to the residual state with the same slope as that of the peak. Line (2) is the new yield surface during softening when the residual tension cut-off gradually decreases to zero leading to the development of shear bands.

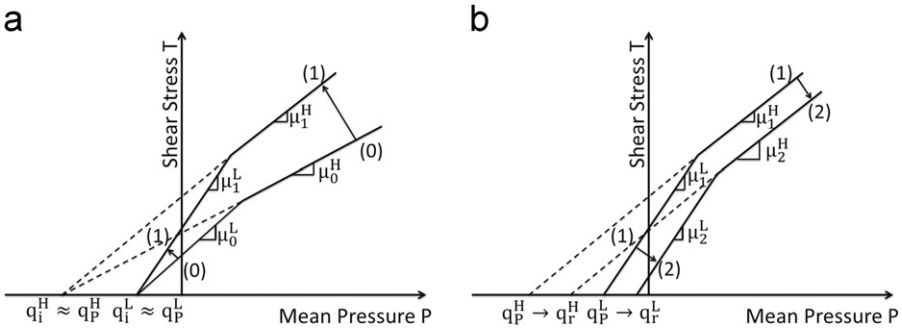

Fig. 4. (a) Hardening and (b) softening of the bilinear Mohr–Coulomb model (Sulem et al., 1999).

3.3. Friction hardening

Plotting the initial yield points versus peak stress for all the tests in T–P space gives the yield functions at initial yielding and at peak strength. The plot gives an indication in dividing the data into two lines: low effective confining stress (LECS) and high effective confining stress (HECS). The data are fitted using a bilinear curve whose slopes give the friction coefficient at LECS and HECS.

In measuring plasticity, the hardening parameter rate is defined as

$$\dot{h}_p = \frac{\sqrt{(\dot{e}_z^p)^2 + (\dot{e}_r^p)^2} - \dot{e}_r^p \dot{e}_z^p}{3} \tag{7}$$

The hardening parameter is the cumulative summation of the hardening parameter rates.

Sulem et al. (1999) suggested that the friction angle in the hardening phase can be related to the hardening parameter using the following formulation:

$$\phi = \begin{cases} \sin^{-1}\left(y_0 + \dfrac{(m_1 - m_2 h_p)h_p}{1 + m_0 h_p}\right) & 0 \le h_p \le h_p^P \\ \phi^P & h_p \ge h_p^p \end{cases} \tag{8}$$

To calculate this friction angle one has to obtain q and μ from the peak yield stress. The value of q may change from the initial to peak yield stress, especially at HECS, but the change was found to be insignificant. Assuming q is constant from the initial yield point up to the peak point, the friction coefficient can be calculated based on T and P from the triaxial tests. The friction coefficient is also a function of the mean stress. Sulem et al. (1999) assumed the friction coefficient is a function of the plastic shear strain and a linear function of the mean stress. In this work, two lines are calibrated (one for LECS and another one for HECS) instead of considering the mean stress in the formulation.

3.4. Cohesion softening

In the softening regime, the friction coefficient is assumed to remain constant and equal to the value at the peak strength. However, decrease in the tension cut-off (Sulem et al., 1999) results in decrease in cohesion. The formulation proposed by Sulem et al. (1999) is used in simulating tests on sandstone, which produced poor results. The reason is primarily attributed to the localized deformation in the post-peak regime, which was assumed to be uniform in Sulem's approach. Hence, the method proposed by Vermeer and De Borst (1984) is utilized to describe the cohesion behavior for the softening part. The following functional form is used:

$$c^* = c^P \exp\left[-\left(\frac{h_p - h_p{}^P}{h_c}\right)^2\right] \tag{9}$$

where c^* is the softened cohesion, c^P is the mobilized cohesion at peak, h_p is the hardening parameter, h_p^p is the hardening parameter at peak strength and h_c is a calibration parameter.

3.5. Mobilized dilation angle

Plastic volumetric strain is developed as a result of plastic shear strain. Shear dependency is defined by the dilation angle

$$\sin\psi = \frac{\dot{e}_v^p}{-2\dot{e}_1^p + \dot{e}_v^p} = \frac{de_v^p}{d(-2e_1^p + e_v^p)} \tag{10}$$

Eq. (10) can be used to calibrate the dilation angle directly from test data. Another approach is to use Rowe's dilatancy formula. Rowe (1972) correlated the mobilized dilation angle to the mobilized friction angle by

$$\sin\psi = \frac{\sin\varphi - \sin\varphi_{cv}}{1 - \sin\varphi\,\sin\varphi_{cv}} \tag{11}$$

where φ_{cv} is the constant volume friction angle (Rowe, 1972) which can be calculated from the dilation angle and friction angle at the peak strength in Rowe's formula.

4. Calibration results

Results of the calibration procedure as described in the previous section are elaborated below for the TB and Castlegate sandstones.

4.1. Friction hardening

As stated before, experimental data showed a constant q in the pre-peak phase. q is evaluated from the yield envelope at the peak strength. Next, the pre-peak triaxial data are used in Eqs. (4) and (7) to plot the friction coefficient versus the hardening parameter for LECS and HECS. A correlation is found based on the best fitting curve of Eq. (8). For TB at LECS

$$\mu = \begin{cases} 1.06 + \dfrac{(258 - 1823\, h_p)h_p}{1 + 3203\, h_p}, & 0 \le h_p \le 0.002 \\ 1.12, & h_p \ge 0.002 \end{cases} \quad (12)$$

and at HECS

$$\mu = \begin{cases} 0.65 + \dfrac{(168 - 6543 h_p)h_p}{1 + 680 h_p}, & 0 \le h_p \le 0.003 \\ 0.80, & h_p \ge 0.003 \end{cases} \quad (13)$$

Fig. 5 shows the friction angle versus hardening parameter calculated from Eqs. (5), (12) and (13) for TB.

$$\mu = \begin{cases} 0.819 + \dfrac{(300 - 9060 h_p)h_p}{1 + 1580 h_p}, & 0 \le h_p \le 0.0025 \\ 0.96, & h_p \ge 0.0025 \end{cases} \quad (14)$$

and at HECS

$$\mu = \begin{cases} 0.418 + \dfrac{(80 - 31614 h_p)h_p}{1 + 665 h_p}, & 0 \le h_p \le 0.0011 \\ 0.446, & h_p \ge 0.0011 \end{cases} \quad (15)$$

Fig. 6 shows the friction angle versus hardening parameter calculated from Eqs. (5), (14) and (15) for Castlegate.

4.2. Cohesion softening

For the post-peak regime, it is assumed that the friction angle remains constant at peak-strength. The constant friction angle is used along with cohesion from Eq. (9) in a series of numerical simulations. Several values are tried

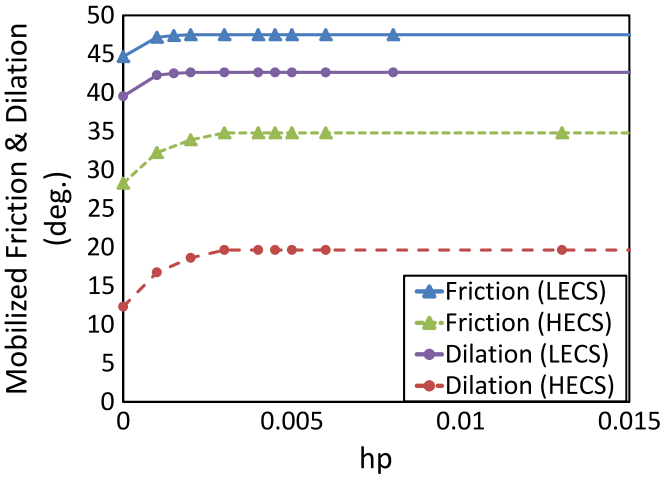

Fig. 5. Friction and dilation angles of TB vs. hardening parameter.

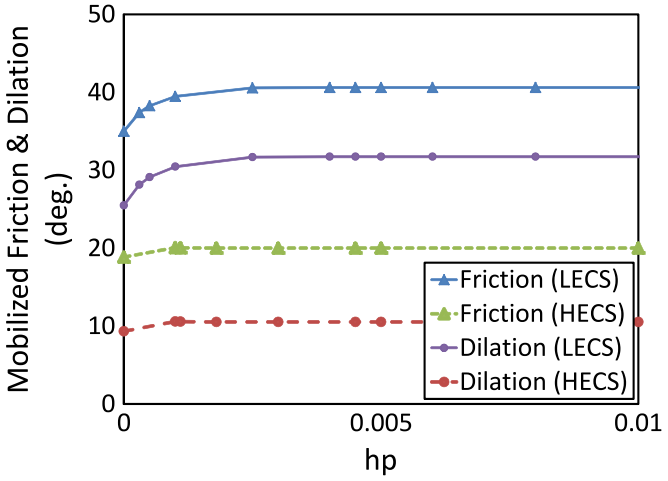

Fig. 6. Friction and dilation angles of Castlegate vs. hardening parameter.

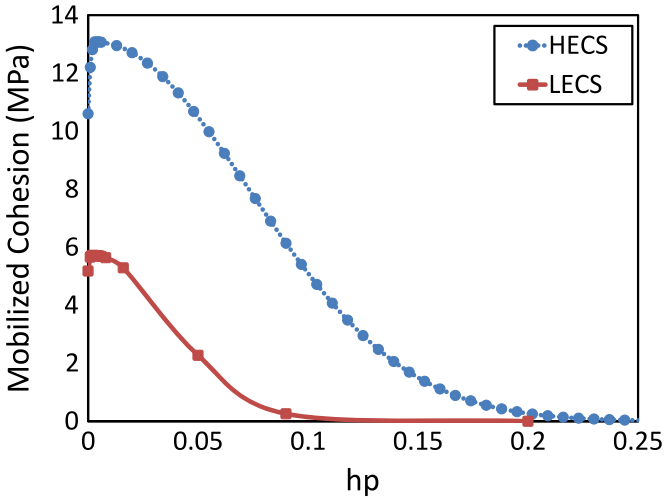

Fig. 7. Mobilized cohesion vs. hardening parameter for TB.

for the calibration parameter h_c. In the end, values of 0.05 and 0.1 for the calibration parameter are found to give the best match at LECS and HECS for TB. The mobilized cohesion is shown in Fig. 7.

In the same way, values of 0.15 and 0.2 for the calibration parameter are found to give the best match at LECS and HECS for Castlegate sandstone. The mobilized cohesion for this sandstone is shown in Fig. 8.

4.3. Mobilized dilation angle

The dilation angle at the peak strength is calculated using Eq. (10), which is then used along with the friction angle at the peak strength to calculate sin φ_{cv} in Eq. (11). Applying this procedure, the average values of 0.12 at LECS and 0.29 at HECS are used for sin φ_{cv} for TB while 0.19 at LECS and 0.17 at HECS are used for Castlegate. The relationships for the friction angle as a function of

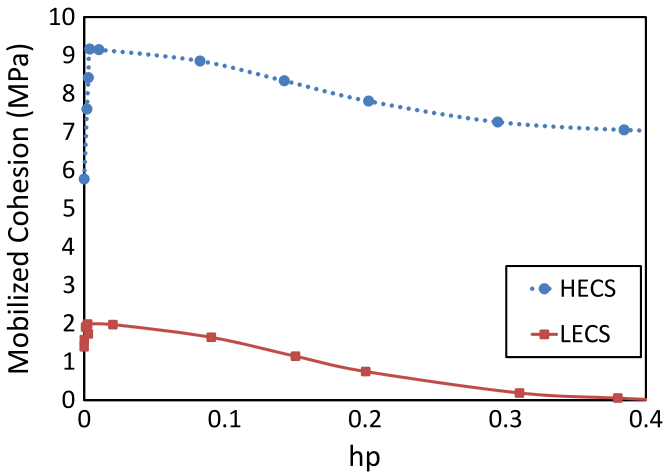

Fig. 8. Mobilized cohesion vs. hardening parameter for Castlegate.

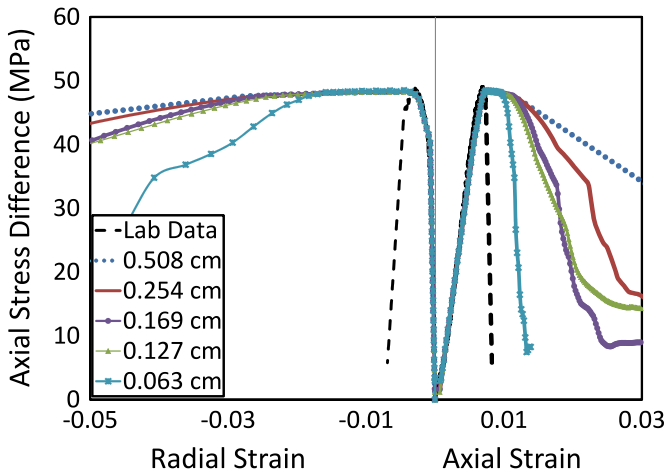

Fig. 9. Mesh-size dependency in the softening regime (legend shows mesh size).

the hardening parameter are already known; therefore, equations for the dilation angle as a function of the hardening parameter can easily be established at LECS and HECS. Since the friction angle is assumed constant in the softening regime, Eq. (11) predicts constant dilation angle after the peak. Figs. 5 and 6 show the calculated dilation angle for TB and Castlegate, respectively.

5. Fracture energy regularization

During the hardening phase, the deformations are nearly uniform. As a result, the whole sample deforms uniformly independent of the mesh design. However, in the softening regime, deformation concentrates in the shear bands. When solving numerically, the shear band resolves itself into the smallest possible thickness, which is one row of elements. The energy released for this localized deformation depends on the size of the shear band (i.e., the size of that one row of deforming elements). The larger the elements, the higher the energy release rate. This difference in energy release for different mesh sizes results in mesh-dependency. This mesh dependency is not observed in the hardening regime because the whole sample deforms uniformly; hence, the same energy is used to deform the sample for different mesh sizes. But once the deformations are localized, the behavior will be different.

Fig. 9 shows the mesh dependency normally observed in the softening regime for TB sandstone. For brevity, only the results of TB sandstone are presented in this part. There are several methods to regularize the continuum to reduce this mesh dependency. One way is to use fracture energy regularization in which one has to include a material characteristic length, l_c^m. The finest acceptable mesh is when $l_c^e = l_c^m$, where l_c^e is the characteristic length of element defined as the diameter of the sphere (circle) having equal volume (area) to the element under consideration.

To use larger element sizes, one needs to change the hardening parameter such that it yields the same fracture energy (Crook et al., 2003)

$$h_p^e = h_p^m \left(\frac{l_c^m}{l_c^e}\right)^n \tag{16}$$

where h_p^m is the material hardening parameter, h_p^e is the modified hardening parameter, and n is a material constant equal to unity when the energy release rate for the fracture growth is constant. The value of $n=0.6$ is calibrated in this work.

Eq. (16) makes the energy release (area under the stress–strain curve) in the softening region the same for different element sizes.

5.1. Shear band thickness

Previous research suggested that the shear band thickness (t_s) should be 10–20 times the mean grain size, d_{50}, of the material (Desrues and Hammad, 1989; Oda and Kazama 1998; Viggiani et al., submitted for publication; Yoshida et al., 1994). Marcher and Vermeer (2001) assembled all the data and correlated them using two lines: $t_s=10d_{50}$ and $t_s=20d_{50}$. They then concluded that most data coincide with the line $t_s=10d_{50}$. They also reported that the data falling on this line were obtained by more reliable measurement techniques such as thin-slice and X-ray methods. Hence, we assume the shear band thickness is about 10 times the mean grain size.

5.2. Characteristic length

The mesh size is selected so that the same experimental shear band thickness is produced numerically. It is important to accurately reproduce the thickness of the shear band to avoid, or at least to reduce, the mesh dependency of the results in the softening phase. In other words, the size of the elements is selected such that the actual size of the shear band is reproduced numerically. The material characteristic length, l_c^m, has been reported to be equivalent

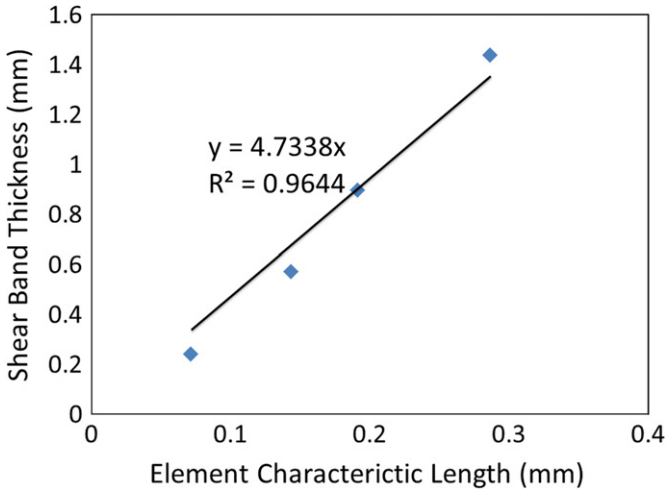

Fig. 10. Dependency of numerically produced shear band thickness on the characteristic length.

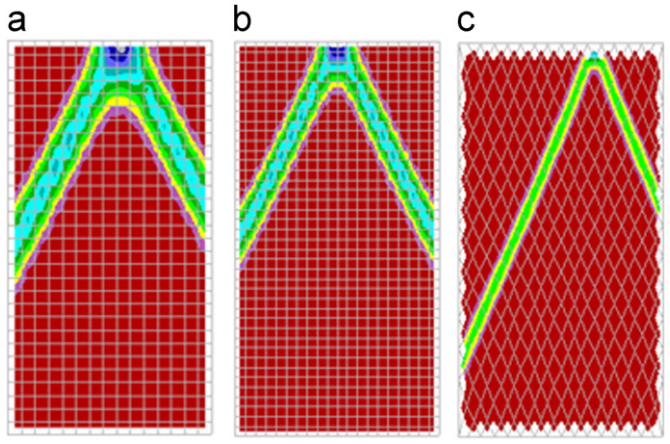

Fig. 11. Plastic strain contours for different mesh designs: (a) coarse mesh, (b) fine mesh and (c) oriented mesh.

to the shear band thickness (Nouri et al., 2009). However, this assumption is valid as long as the shear band is produced within one row of elements only. Fig. 10 shows a linear dependency of the numerically produced shear band thickness on the material characteristic length for a common rectangular element. It is concluded that the shear band would be approximately 4.73 times the characteristic length for rectangular shaped elements. Hence, for a rectangular element

$$l_c^m = \frac{t_s}{4.734} = \frac{10\ d_{50}}{4.734} = 2.11\ d_{50} \tag{17}$$

Since this value is only an average value between a limited number of tests and since localization usually occurs diagonally with an inclination of the failure angle, the shear band will still be slightly thicker than the real physical size (Fig. 11a and b). Therefore, oriented mesh geometry is used to reduce the size of the shear band to one row of elements only (Fig. 11c). Several numerical experiments demonstrated that if the angle of oriented mesh is the same as that of the failure angle, i.e., $45+(\varphi+\psi/4)$, the shear band will be limited to one element row, and the material characteristic length will be the same as the shear band thickness (Fig. 11c). If the effect of mesh shape was not considered on the characteristic length, we would have had different results even with regularization.

The oriented mesh is considered to be the base case here, and all the other simulations are compared with this base case. A plane strain model with regular rectangular mesh (both coarse and fine) is simulated and compared with the base case. An axisymmetric model is also performed and compared with the base case.

6. Back-analysis of triaxial tests

Back-analyses of the tests are performed using FLAC software. Various approaches have been taken to capture the stress–strain behavior of the reservoir rock. It is common to simulate triaxial experiments using an axisymmetric configuration; however, an axisymmetric configuration does not allow localization of deformation. A plane strain configuration was used to capture localization. The results were later compared with those from using an axisymmetric configuration. Fracture energy regularization is applied to remove mesh dependency.

6.1. Mesh size

The triaxial samples are 1 in. (2.54 cm) in diameter and 2 in. (5.08 cm) in length. Mesh sizes of 0.2 in. (0.508 cm), 0.1 in. (0.254 cm), 0.067 in. (0.169 cm) and 0.05 in. (0.127 cm) are used for the rectangular mesh. The mean average grain size of TB is 0.0055 in. (0.14 mm). Hence, the characteristic length would be approximately 0.0116 in. (0.2957 mm) and 0.055 in. (1.4 mm) for the rectangular and oriented mesh, respectively.

6.2. Boundary conditions

The bottom boundary of the finite element mesh is fixed in the y (vertical) direction. The radial and axial loads are applied on the boundaries, and then a small velocity in the vertical direction is applied on the top boundary as directed by the experimental procedure.

In the laboratory experiments, two steel platens are used at the top and bottom of the rock samples. Axial loads are directly applied on the platens. The surfaces between the steel and the rock are usually lubricated to avoid end effects. As a result, the platens are assumed to be frictionless.

6.3. Back-simulation results

As described previously, plane strain conditions with oriented mesh in the simulation are used in the simulation. The elasto-plastic material properties are calculated as presented in Section 4. Tables of cohesion, friction and

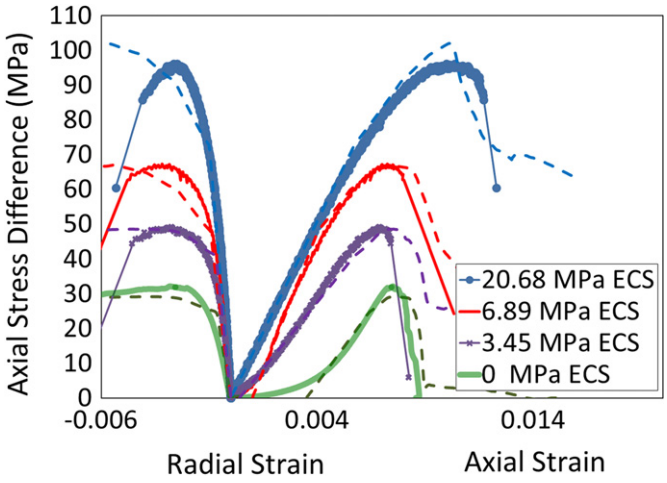

Fig. 12. Comparison of simulated results with triaxial experiments for TB sandstone (simulated results are shown with dashed lines).

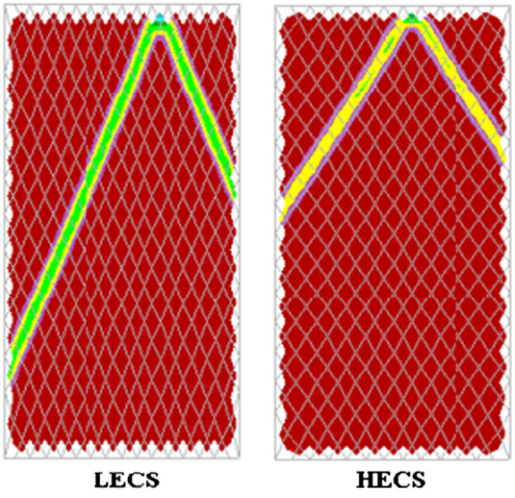

Fig. 13. Plastic strain contour showing the formation of shear band.

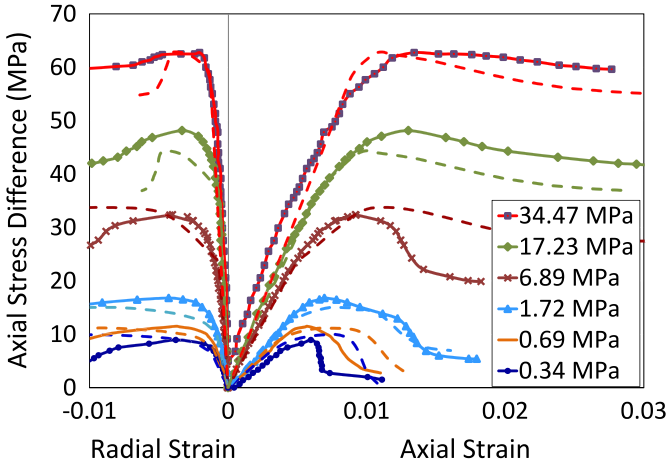

Fig. 14. Comparison between simulation and triaxial test results for Castlegate sandstone (simulated results are shown with dashed lines).

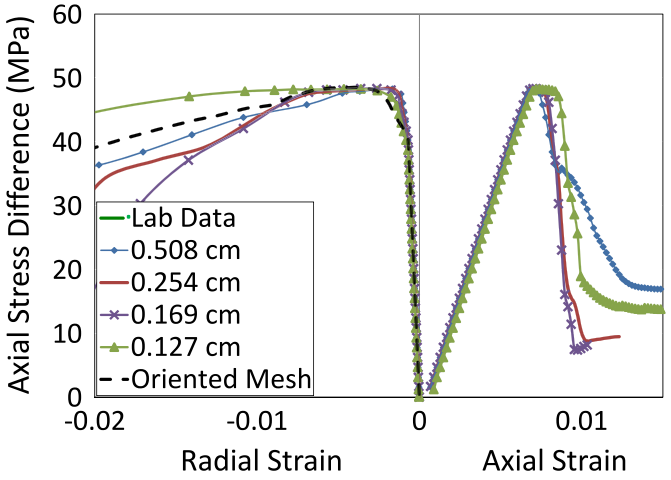

Fig. 15. Comparison between simulations and experimental observations for different mesh designs (confining stress = 3.45 MPa, legend shows mesh size).

dilation angle versus hardening parameter are used as the input data in the model. The results are presented in Figs. 12 and 13.

It should be noted that radial displacement measurements are not uniform along the sample after the onset of localization. In other words, radial displacements at different heights and radial angles are different. Two experimental radial strain measurements are located at mid-height 90° apart to compare the experimental radial displacements with numerical calculations. Hence, obtaining a match for the radial strains is not carried out in this calibration. Actually, the radial displacements for plane strain conditions are the maximum displacements possible. Accurate calculation of radial strain requires a 3D analysis, and even then, it is difficult to compare radial strain with the laboratory measurements taken at only two measurement points.

In addition to TB, the calibration and simulation method was applied to six Castlegate tests as well. The results are shown in Fig. 14.

6.4. *Effect of mesh design*

Regular coarse mesh and fine mesh with fracture energy regularization are also simulated using the calibrated data and are compared with the base case (i.e., oriented mesh). Plane strain is assumed in all the models. The results are shown in Fig. 15 for 3.45 MPa (500 psi) effective confining stress.

Compared to Fig. 9, not only is the mesh dependency largely reduced, but also the results are closer to the experimental data.

Selecting the characteristic length equal to the shear band thickness regardless of the mesh shape does not result in good matches. Fig. 16 demonstrates the results for such a case.

Differences in the softening part of each simulation are expected. As shown in the figures, the results are highly dependent on the mesh design and the choice of characteristic length. Utilization of the fracture energy regularization method with the angular mesh ensured objective calibration. For simpler simulations, such as a triaxial test it is most

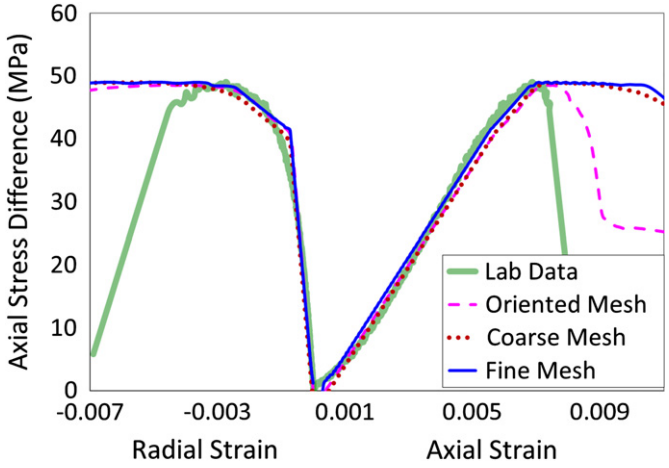

Fig. 16. Comparison between simulations and experimental observations for different mesh designs without proper selection of characteristic length (confining stress = 3.45 MPa).

favorable to apply oriented mesh and to select the elements size equal to the shear band size so that the actual shear band thickness can be captured. However, in more complicated applications it is very difficult, if not impossible, to align the mesh with the shear band as it requires pre-knowledge of the shear band location and thickness. In general, as long as the material characteristic length is selected based on the mesh size and shape the results will be adequately well.

6.5. *Axisymmetric model*

The triaxial tests are cylindrical, but the plane strain simulations are rectangular. The difference in the configuration and assumption of plane strain had an impact. Simulation of triaxial experiments is usually carried out using an axisymmetric assumption. However, this assumption does not allow localization, which is commonly seen in the post-peak regime, to occur. Note that a cylinder with a cutting plane is no longer axisymmetric. Fig. 17 demonstrates the axisymmetric mesh of one-half sample section.

The simulation results for 3.45 MPa confining stress are shown in Fig. 18. This model predicts better radial strains as the radial strains in the axisymmetric model are somehow the average strains. Since the axisymmetric model cannot capture localization of deformation, the displacements are completely different from those of the plane strain models. Fig. 19 shows the displacements in the plane strain and the axisymmetric models. The modeling approach is, therefore, seem to have a high impact on the calibration and the numerical response.

7. Summary and conclusions

This paper presented a detailed approach for calibrating a Mohr–Coulomb model for simulating the degrading behavior of sandstones. The procedure is demonstrated by calibrating the model for two sets of triaxial testing data.

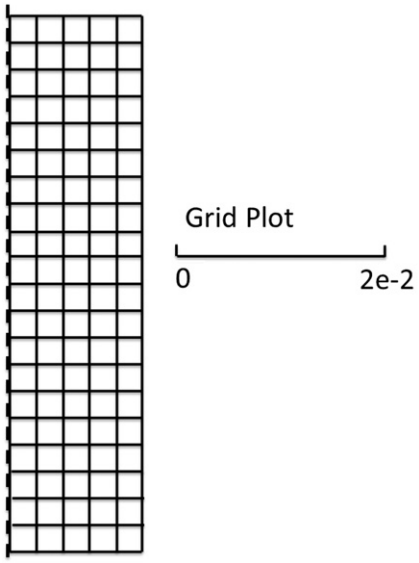

Fig. 17. Axisymmetric mesh.

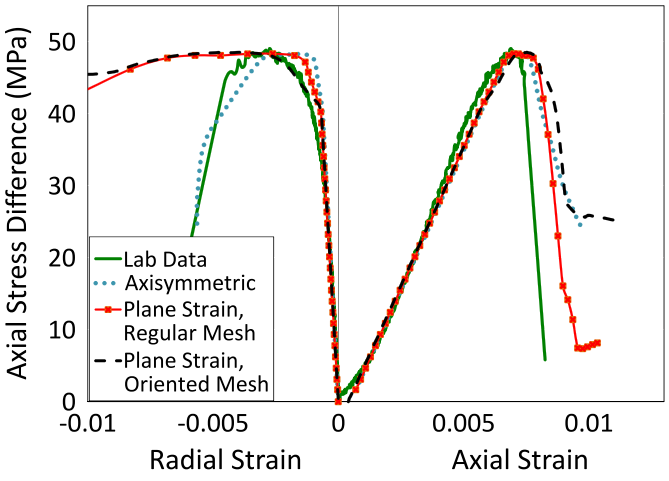

Fig. 18. Comparing results of the axisymmetric with plane strain model (confining stress = 3.45 MPa).

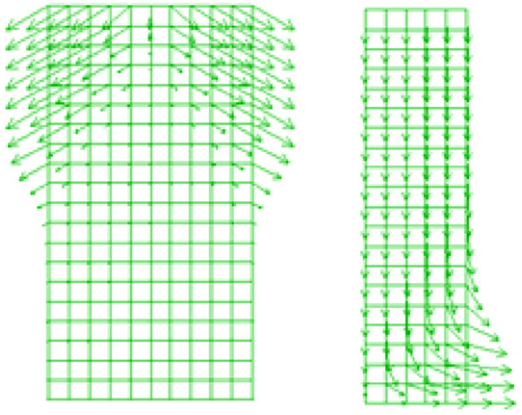

Fig. 19. Comparison of displacement between (a) a plane strain and (b) an axisymmetric model for the same mesh size (confining stress = 3.45 MPa).

The calibrations and back-simulation of TB and Castlegate sandstones show:

- The bilinear Mohr–Coulomb model with friction-hardening/cohesion-softening is capable of reproducing sandstone behavior.
- The friction hardening formula offered by Sulem et al. (1999) along with constant tension cut-off was found to be adequate in the strain-hardening phase.
- The cohesion softening formula along with constant friction angle as offered by Vermeer and De Borst (1984) combined with a plane strain modeling of triaxial tests with angular mesh was found to simulate the softening phase reasonably well.
- The oriented mesh inclined at the failure angle results in the formation of shear band in one element row. This is most favorable in shear band simulations if the elements size is selected equal to the shear band size so that the actual shear band thickness can be captured.
- The fracture energy regularization method is found to be capable of reducing mesh dependency. However, the appropriate choice of characteristic length is essential. To have effective regularization, it is important to consider the shape of the mesh in the calculations of the characteristic length. The characteristic length for each mesh can be chosen in such a way that produces the shear band thickness numerically.
- Although axisymmetric assumption yields the best match for stress–strain curve when deformations are uniform, it does not allow capturing shear band formation and development in the softening phase. Plane strain model is a better choice and is the only way to model shear bands in 2D simulations.

Acknowledgements

The authors would like to express their gratitude to BP for their financial support and permission to use the experimental data. The financial support provided by NSERC is also acknowledged.

References

Bazant, Z.P., Oh, B.H., 1983. Crack band theory for fracture of concrete. Materials and Structures (RILEM, Paris) 16, 155–177.

Crook, T., Willson, S., Guo, Yu J., Owen, R., 2003. Computational modeling of localized deformation associated with borehole breakout in quasi-brittle materials. Journal of Petroleum Science and engineering 38, 177–186.

Desrues, J., Hammad, W., 1989. Shear banding dependency on mean stress level in sand. In: International Workshop: Numerical Methods for Localization and Bifurcation of Granular Bodies, Gdansk-Sobieszewo, pp. 57–67.

Marcher, T., Vermeer, P.A., 2001. Macromodelling of softening in non-cohesive soils. In: Vermeer, P.A. (Ed.), Continuous and Discontinuous Modelling of Cohesive-Frictional Materials. Springer, Berlin, pp. 89–110.

Nouri, A., Kuru, E., Vaziri, H., 2009. Elastoplastic modelling of sand production using fracture energy regularization method. Journal of Canadian Petroleum Technology 48 (4), 64–71.

Oda, M., Kazama, H., 1998. Microstructure of shear bands and its relation to the mechanisms of dilatancy and failure of dense granular solis. Géotechnique 48 (4), 465–481.

Pietruszcak, S.T., Mroz, Z., 1981. Finite element analysis of deformation of strain softening. International Journal of Numerical Methods in Engineering 17 (3), 327–334.

Rowe, P.W., 1972. Theoretical meaning and observed values of deformation parameters for soils. In: Proceedings of the Roscoe Memorial Symposium on Stress–Strain Behaviour of Soils, Cambridge, Foulis, Henley-on-Thames, pp. 143–194.

Schanz T., Vermeer P.A. Bonnier P.G., 1999, The Hardening Soil Model: Formulation and Verification, Beyond 2000 in Computational Geotechnique.

Sluys L.J., 1992. Wave Propagation, Localisation and Dispersion in Softening Solids. Ph.D. Thesis. Delft Institute of Technology.

Sulem, J., Vardoulakis, I., Papamichos, E., Oulahna, A., 1999. Elasto-plastic modeling of Red Wildmoor sandstone. Mechanics of Cohesive-Frictional Materials 4, 215–245.

Vermeer, P.A., De Borst, R., 1984. Non-associated plasticity for soils, concrete and rock. Heron 29, 1–62.

Viggiani, G.Küntz, M., Desrues, J.. Does shear banding in sand depend on grain size distribution? In: Proceedings of the CDM2000 Stuttgart, International Symposium on Continuous and Discontinuous Modelling of Cohesive Frictional Materials, Springer, submitted for publication.

Yoshida, T., Tatsuoka, F., Siddiquee, M.S.A., Kamegai, Y., Park, C.-S., 1994. Shear banding in sands observed in plane strain compression. In: Chambon, Desrues, Vardoulakis (Eds.), Localisation and Bifurcation Theory for Soils and Rocks, pp. 165–179.